A 4D-Var inversion system based on the icosahedral grid model (NICAM-TM 4D-Var v1.0): 1. Off-line forward and adjoint transport models
Yosuke Niwa
Hirofumi Tomita
Masaki Satoh
Ryoichi Imasu
Yousuke Sawa
Kazuhiro Tsuboi
Hidekazu Matsueda
Toshinobu Machida
Motoki Sasakawa
Boris Belan
Nobuko Saigusa
2016-10-11
journal article
en
10.5194/gmd-2016-231
Author(s) 2016. CC-BY 3.0 License.

ce

1 Introduction

We have developed a new 4-dimensional variational (4D-Var) inversion system for estimating surface fluxes of greenhouse gases (GHGs: present primarily targets are carbon dioxide (CO_2) and methane (CH_4)). The new system is referred to as NICAM-TM 4D-Var. It consists mainly of forward and adjoint transport models and an optimization scheme. This paper
5   presents derivation of the transport models and evaluate their performances. The accompanying paper (Niwa et al., 2016) describes the optimization scheme and demonstrates the application of the new system to an atmospheric CO_2 inversion problem.

The 4D-Var inversion method has evolved over the years to achieve higher spatiotemporal resolution in inverse calculations of various atmospheric trace gas measurements (Rödenbeck, 2005; Chevallier et al., 2005; Baker et al., 2006; Meirink et al.,
10   2008; Basu et al., 2013; Wilson et al., 2014; Liu et al., 2014) that include continuous measurements at the surface, as well as aircraft (Machida et al., 2008; Sawa et al., 2015; Matsueda et al., 2015) and satellite observations (e.g. Yokota et al., 2009). The 4D-Var is an iterative method requiring model simulations many times, not only forward but also backward using an adjoint model. Moreover, a global inversion calculation of an atmospheric greenhouse gas requires a long time analysis window (∼20 years) owing to the gas' long atmospheric lifetime (Chevallier et al., 2010), resulting at least hundreds of years of model
15   simulations. This motivates us to develop ways of making computation more efficient.

For GHG simulations, there are two types of atmospheric transport models: one is on-line (e.g. Patra et al., 2009) and the other is off-line (e.g. Kawa et al., 2004; Huijnen et al., 2010). On-line models include atmospheric general circulation models (AGCMs) which incorporate passive tracers of GHGs and simulate their movements. Off-line models are those that simulate transport of tracer gases using archived meteorological data (e.g. temperature, wind velocity, humidity). Therefore, an off-line
20   model is computationally much more efficient than an on-line model and hence is favored for the 4D-Var calculation. However, archived meteorological data usually consist of reanalysis data with limited spatiotemporal resolution. Furthermore, reanalysis data are not physically consistent with each other (Stohl et al., 2004). Therefore, in off-line transport calculation, reanalysis wind data should be modified in advance to restore the dynamical consistency with pressure tendencies, otherwise the tracer mass cannot be conserved (Heimann and Keeling, 1989; Heimann, 1995; Bregman et al., 2003).

25   An adjoint model integrates variables backward in time to calculate sensitivities of a certain scalar variable against model parameters (Errico, 1997), with applications to data assimilation and inversion analyses. Furthermore, the adjoint sensitivity could be a powerful tool to diagnose tracer transport mechanisms (e.g. Vukićević and Hess, 2000). For GHG inverse analyses, the atmospheric processes are considered to be all linear, with CO_2 and CH_4 transported as passive tracers and CH_4 loses calculated by simple linear equations with prescribed hydroxyl (OH) and chlorine (Cl) radicals and $O(^1D)$ (Patra et al., 2011). But
30   in practice, non-linearity is introduced into the discretized model, hampering the development of an adjoint model. One prominent example is the discretization of an advection scheme. An advection scheme with higher than first order accuracy must employ a non-linear algorithm to preserve tracer monotonicity (Godunov, 1959). Therefore, an advection scheme often uses a non-linear flux limiter or fixer that depends on tracer quantities, introducing non-linearity and discontinuity. However, the direct adjoint of such a non-linear code is computationally inefficient for a long simulation, because it requires several check-

points from which time forward simulations are restarted to restore tracer quantities at every model time step. Furthermore, it has been found that such an adjoint model is ill-behaved due to the discontinuity (Thuburn and Haine, 2001; Vukićević et al., 2001). Therefore, alternative approaches have been proposed at the expense of linearity or the accuracy of numerical scheme (Vukićević and Hess, 2000; Vukićević et al., 2001; Sandu et al., 2005; Hourdin and Talagrand, 2006; Hakami et al., 2007; Gou

5 and Sandu, 2011; Haines et al., 2014). Most studies use either the "discrete adjoint" or "continuous adjoint". However, which approach performs better is still controversial. The discrete adjoint is linear but reduces the accuracy of the numerical scheme, while the continuous adjoint is non-linear but maintains the numerical accuracy.

In this study, we have achieved a level of computational efficiency to conduct a 4D-Var inversion of atmospheric GHGs using off-line forward and adjoint models. The off-line model is closely linked to the AGCM of Nonhydrostatic ICosahedral

10 Atmospheric Model (NICAM: Tomita and Satoh, 2004; Satoh et al., 2008, 2014). In fact, the model can be considered as an off-line version of the on-line transport model of NICAM-based Transport Model (NICAM-TM: Niwa et al., 2011a, b). In the off-line model, tracer transport is calculated in the same way as in the on-line model, but driven by meteorological data provided from the AGCM run of NICAM in which winds fields are nudged toward reanalysis data. Compared to the reanalysis data, the physical and dynamical consistency in the nudged AGCM data is maintained. Furthermore, the use of the AGCM

15 enables us to change the spatiotemporal resolution. Similar AGCM-based off-line models have been developed by previous studies (Hourdin et al., 2006; Yumimoto and Takemura, 2013). In fact, the off-line NICAM-TM has already been used in a CO_2 inversion using the conventional matrix calculation method (Niwa et al., 2012). In this study, we examine the relative impact of meteorological driver with different temporal resolution in each of the transport processes (advection, vertical diffusion and cumulus convection) on model accuracies. Maintaining the same degree of flexibility in the time resolution of the off-line

20 forward model, we develop a new adjoint model. The new adjoint model can be run in the discrete or continuous mode. In order to achieve the exact adjoint relationship with its corresponding forward model, the discrete adjoint method switches off the non-linear flux limiter in the advection scheme, while the continuous adjoint utilizes the flux limiter to give preference to monotonicity over the adjoint exactness.

Because thinning (i.e., reducing time resolution, resulting in a decreased number of data points) of the meteorological

25 data might introduce some additional model errors in the off-line calculation, we evaluate those errors by comparing CO_2 concentrations simulated by the off-line model with those by the one-line model. In that evaluation, we test various temporal resolutions of the meteorological data, which are separately determined for each transport process. Also, we validate the fundamental property of the adjoint model and demonstrate the utility of the adjoint sensitivity in a back-trajectory analysis.

2 Methods

30 ### 2.1 NICAM

The horizontal grid of NICAM has a distinctive structure. Different from the conventional latitude-longitude grid models, it has a quasi-homogenous grid distribution produced from an icosahedron obtained by a recursive division method (Stuhne and Peltier, 1996). This avoids the pole problem and facilitates high-resolution simulations. Therefore, the dynamical core of

NICAM is constructed with nonhydrostatic equations (Tomita and Satoh, 2004). Furthermore, the model program is designed for an efficient parallel computation with Message Passing Interface (MPI) libraries (Tomita et al., 2008; Kodama et al., 2014). In fact, NICAM has been used for global nonhydrostatic high-resolution simulations with 14 km to 850 m grid resolutions (Miura et al., 2007; Miyamoto et al., 2013; Miyakawa et al., 2014). Nonetheless, in this study, we use a moderate resolution to

5   reduce the high computational cost associated with the GHG inversion that requires repeated long-term simulations.

We set the horizontal resolution at "glevel-5" (Fig. 1). The number 5 denotes the number of division of the icosahedron. NICAM adopts the finite volume method (Tomita and Satoh, 2004), whose control volume is a shaped pentagon at twelve vertices of the original icosahedron and hexagon at other grids (Fig. 1b). Those control volumes are constructed by connecting mass centers of the triangular elements that are produced by the recursive division of the icosahedron (Fig. 1a). The mean grid

10   interval of glevel-5 is approximately 240 km. Although this horizontal resolution is much coarser than the high-resolutions that NICAM mainly targets, it is still comparable to or finer than the resolutions used in previous GHG inversion studies (e.g. Peylin et al., 2013).

Because the dynamical core is constructed with the finite volume method, NICAM achieves the consistency with continuity (CWC: Gross et al., 2002) for the tracer transport (Satoh et al., 2008; Niwa et al., 2011b), which cannot be achieved in spectral

15   AGCMs (Jöckel et al., 2001). Owing to this CWC property, tracer mass is perfectly conserved without any numerical mass fixer. Indeed, motivated by the CWC property, atmospheric transport studies have been conducted using NICAM-TM with glevel-5. The model reproduces reasonably well the synoptic scale and vertical variations of radon (^{222}Rn) and the inter-hemispheric gradients of sulfur hexafluoride (SF_6) at the surface and in the upper troposphere (Niwa et al., 2011b, 2012).

The model configuration in this study is basically the same as the one described in Niwa et al. (2012), except for the

20   cumulus parameterization. The cumulus parameterization scheme is changed from Arakawa and Schubert (1974) to Chikira and Sugiyama (2010). The number of vertical model layers is 40, 12 layers of which exist below about 3 km. The top of the model domain is at about 45 km. The tracer advection process is calculated with the scheme of Miura (2007), and the vertical turbulent mixing is calculated with the MYNN Level 2 scheme (Mellor and Yamada, 1974; Nakanishi and Niino, 2004; Noda et al., 2010). The model time step of glevel-5 is 20 min., both for the on-line and off-line calculations. For the nudging used

25   in the on-line calculation, we use the 6-hourly horizontal wind velocities of the Japan Meteorological Agency Climate Data Assimilation System (JCDAS) reanalysis data (Onogi et al., 2007).

2.2   Off-line NICAM-TM

As is the case in the on-line model, the off-line model integrates tracer mass ρq (ρ is air mass density and q is tracer mixing ratio) as

30   $$\frac{\partial \rho q}{\partial t} = \nabla \cdot (\rho \mathbf{v} q) + \frac{\partial}{\partial z}\left[\rho K_v \left(\frac{\partial q}{\partial z}\right)\right] + f_c\left(\rho, q_w, T, M_B, q\right), \tag{1}$$

where ∇ and $\mathbf{v}$ are the three-dimensional divergence operator and wind vector, respectively, and K_v is the vertical diffusion coefficient. On the right hand side of the equation, the first and second terms represent the grid scale tendency of advection and the sub-grid scale one of vertical diffusion, respectively. The third term f_c denotes the sub-grid scale tendency of cumulus

convection, determined by ρ and the mixing ratios of water substances (q_w), temperature (T), and cumulus base mass flux (M_B).

Table 1 shows the archived meteorological parameters that drive the off-line model. Integrative time resolutions of these parameters are thinned out (i.e., reduced) from the model time step interval of 20 min. to several hours. In this study, we conduct sensitivity of the model results to changes in the time resolution of each of the driving meteorological transport variables (advection, vertical diffusion and cumulus convection) (Section 3.2).

In the archiving of the meteorological data, averaged values are saved for the air mass flux $\mathbf{V}$ ($= \rho \mathbf{v}$), while instantaneous values are saved for other meteorological parameters. The averaging of $\mathbf{V}$ is intended to preserve the CWC property. Originally, NICAM calculates the tracer advection using time-averaged air mass fluxes that are derived from air mass fluxes at a shorter time interval. The tracer advection is calculated with the Euler scheme, while momentums are calculated at a shorter time interval using the Runge-Kutta scheme. The time-averaged air mass flux retains the CWC property (Satoh et al., 2008; Niwa et al., 2011b). The off-line model uses air mass fluxes that are further averaged for the thinning interval as

$$\overline{\mathbf{V}}^t = \frac{1}{N} \sum_{i=1}^{N} \mathbf{V}^{t+i\Delta\tau}, \tag{2}$$

where Δt is the thinning interval and $\Delta\tau$ is the model time step, and N is the integer defined as $N = \Delta t / \Delta\tau$. The off-line calculation, whose time step is the same as that of the on-line, uses the above repeatedly during N steps from t to $t + \Delta t$ as

$$(\rho q)^{t+(i+1)\Delta\tau} = (\rho q)^{t+i\Delta\tau} + \Delta\tau \left(\nabla \cdot \overline{\mathbf{V}}^t q^{t+i\Delta\tau} \right). \tag{3}$$

In order to preserve CWC, ρ is simultaneously integrated with the same time-averaged air mass flux as

$$\rho^{t+(i+1)\Delta\tau} = \rho^{t+i\Delta\tau} + \Delta\tau \left(\nabla \cdot \overline{\mathbf{V}}^t \right) + \alpha, \tag{4}$$

where α is the modification term. If $\alpha = 0$, the Lagrangian conservation ($dq/dt = \partial q/\partial t + \mathbf{v} \cdot \nabla q = 0$) is achieved, which can be easily shown by substituting (4) to (3). In practice, α is nonzero and the Lagrangian conservation is not strictly satisfied owing to evaporation and precipitation (note that ρ includes not only dry air but also water substances). This α is calculated as

$$\alpha = \frac{1}{N} \left(\rho^{t+\Delta t} - \rho^t - \Delta t \left(\nabla \cdot \overline{\mathbf{V}}^t \right) \right), \tag{5}$$

so that the integrated ρ with Eq. (4) after N steps coincides with $\rho^{t+\Delta t}$ that is provided from the on-line calculation. The other meteorological parameters (K_v, q_w, T and M_B) are linearly interpolated from the thinned interval steps to the model time steps.

2.3 Adjoint NICAM-TM

When $\mathbf{M}$ represents a forward model matrix and $\mathbf{a}$ and $\mathbf{b}$ are arbitrary vectors, an adjoint model matrix $\mathbf{M}^*$ satisfies $\langle \mathbf{a}, \mathbf{M}\mathbf{b} \rangle = \langle \mathbf{M}^*\mathbf{a}, \mathbf{b} \rangle$, where $\langle ., . \rangle$ is an inner product. In the usual case, the inner product is defined as $\langle \mathbf{a}, \mathbf{b} \rangle = \mathbf{a}^T \mathbf{b}$; therefore, $\mathbf{M}^*$ is equivalent to $\mathbf{M}^T$. In practice, $\mathbf{b}$ represents mixing ratio or surface flux and $\mathbf{a}$ is its adjoint variable. An adjoint model integrates adjoint variables backward in time to calculate sensitivities.

An adjoint model is constructed based on the above off-line forward model. The adjoint model reads the archived meteorological data in the same way as the off-line model does, but in reverse. Furthermore, similar to Eq. (4), ρ is simultaneously integrated with the reversed winds and $-\alpha$ in place of α.

For the vertical diffusion and cumulus convection processes, we use the discrete adjoint approach in which linear program codes are simply transposed. For the advection process, we employ both the discrete and continuous approaches. In the discrete adjoint approach, we give up the monotonicity. In NICAM, the tracer monotonicity is achieved by the use of the flux limiter of Thuburn (1996) (Miura, 2007; Niwa et al., 2011b). All the transport calculations other than the flux limiter are linear. Therefore, we obtain a completely linear forward model by just switching off the flux limiter. From that linear forward model, we construct the adjoint model by simply transposing the linear codes. Because of the linearity, this adjoint model is expected to have the exact adjoint relationship with the forward model (with the flux limiter off), as proven in Section 3.4. The relationship is expressed as

$$\left(\mathbf{M}\mathbf{x}\right)^{\mathrm{T}}\mathbf{y} = \mathbf{x}^{\mathrm{T}}\left(\mathbf{M}^{\mathrm{T}}\mathbf{y}\right), \tag{6}$$

where $\mathbf{x}$ and $\mathbf{y}$ represent the model input parameter vector and the observation vector, respectively. By giving up the monotonicity, however, the discrete adjoint produces negative (or oscillatory) sensitivities and reduces the model accuracy to some extent.

In the second approach, continuous adjoint model is developed by discretizing the continuous adjoint equation (Sandu et al., 2005; Hakami et al., 2007; Gou and Sandu, 2011). In this approach, the flux limiter can be employed not only in the forward model, but also in the adjoint model, keeping the tracer concentrations or sensitivities positive (or non-oscillatory). However, due to the non-linearity of the flux limiter, the adjoint relationship is no longer inexact. The continuous adjoint equation of advection is written as

$$-\frac{\partial q^*}{\partial t} = \nabla \cdot \left(\mathbf{v}q^*\right), \tag{7}$$

where q^* is the adjoint variable for q. Equation (7) can be derived by the Lagrange's method of undetermined multipliers and partial integral from the advection part of Eq. (1) (detail derivation can be found in Sandu et al. (2005)). Let $\tilde{q}^* = q^*/\rho$, and we obtain

$$-\frac{\partial \rho \tilde{q}^*}{\partial t} = \nabla \cdot \left(\rho \mathbf{v}\tilde{q}^*\right). \tag{8}$$

By comparing with Eq. (1), we find that we can reuse the divergence operator of the forward code by reversing the wind direction and integrating it backward in time. Thus, we can employ the non-linear flux limiter to maintain the monotonicity of $\tilde{q}^*$.

All the adjoint codes are manually written, achieving numerical efficiency of the model. Some studies use an automatic differentiation tool to readily make the adjoint model, but it sometimes makes the model numerically inefficient. Furthermore, we retain the parallel computational ability of NICAM, allowing significant savings in computational time.

2.4 CO$_2$ flux data

For the validation of the off-line forward model, we simulate atmospheric CO$_2$ for the year 2010. For the surface boundary CO$_2$ flux input to the model, we use the inversion flux of Niwa et al. (2012) that is optimized for atmospheric CO$_2$ concentrations for 2006–2008. The inversion (posterior) flux consists of prior flux datasets and monthly flux adjustments derived from the observations. In this study, we replace the prior flux datasets with those for 2010 other than the climatological air-sea exchange data from Takahashi et al. (2009); we use the monthly data of fossil-fuel emission from the Carbon Dioxide Information Analysis Center (CDIAC) (Andres et al., 2013), of biomass burning emission from the Global Fire Emissions Database ver. 3.1 (van der Werf et al., 2010) and of terrestrial biosphere net ecosystem production (NEP) from the Carnegie-Ames-Stanford Approach (CASA) model (Randerson et al., 1997). To represent the diurnal variation of the terrestrial biosphere flux, we redistribute the monthly CASA NEP into 3-hourly fluxes by the same method as Olsen and Randerson (2004) using 2 m height air temperature and downward shortwave radiation data of JCDAS for 2010. Although the integrated surface CO$_2$ flux input to the model does not necessarily represent the actual flux variations in 2010, the overall resulting atmospheric CO$_2$ concentration field is consistent with the actual observed CO$_2$ concentrations, permitting an effective evaluation of the model transport performance. The initial concentration field is also made by the inversion flux through the simulation for 2003–2009.

3 Results

3.1 Computational cost

All the simulations are performed on PRIMEHPC FX100 with MPI parallelization by 10 nodes (each node has 32 cores). For the one-year-long sensitivity test simulation discussed below, the off-line forward model requires only 7 min., while the on-line model requires about 70 min. Therefore, the off-line model is 10 times faster computationally than the on-line model. With the corresponding adjoint calculation requiring about additional 7 min., the 4D-Var calculation is demonstrated to be reasonably feasible.

3.2 Evaluation of the data thinning error

As described in Section 2.2, the off-line model can use a different data-thinning interval for each transport process. In order to determine an appropriate data-thinning interval, we perform five sensitivity runs (A6V6C6, A3V6C6, A3V6C3, A3V3C3, A3V1C3), changing the interval from 6 hours to 1 hour, as shown in Table 2. In addition, we test A3V1C3 with the flux limiter in the advection scheme switched off (which is the counterpart of the discrete adjoint).

Figure 2 shows zonal mean pressure-latitude cross-section of the root-mean-square difference (RMSD) in CO$_2$ concentration between the off-line and on-line models. The RMSD value is calculated from hourly model output. The RMSD value represents the error induced only by the data-thinning. Generally, the RMSD values are small even in the coarsest resolution case in which all the transport processes are calculated with 6-hourly data (A6V6C6). In most areas, the RMSDs are less than 1 ppm, indicating that the atmospheric transport is generally well simulated by the 6-hourly resolution. The relative error, which is

defined as RMSD divided by the standard deviation of the concentration variation simulated by the on-line model, is 12.9 and 5.3 % on average at the surface and 300 hPa, respectively (Table 2).

A closer examination shows that the temporal resolution of each transport process affects the spatial distribution of RMSD. As shown in Figs. 2a and b, halving the interval of the advection data from A6V6C6 to A3V6C6 does not significantly

5 reduce RMSDs, with the relative errors at the surface and 300 hPa decreasing slightly to 12.7 (from 12.9) and 4.8 (from 5.3) %, respectively. However, the RMSDs values are noticeably reduced in the mid to upper troposphere by halving the interval of the cumulus convection data from A3V6C6 to A3V6C3, with the relative error in 300 hPa reduced to 3.3 %. This indicates a significant role of cumulus convection on CO_2 concentration variations in the mid to upper troposphere. Furthermore, increasing the temporal resolution of the vertical diffusion coefficient from A3V6C3 to A3V3C3, and to A3V1C3,

10 we find greater RMSD reductions near the surface (Figs. 2d and e). The relative errors at the surface are reduced to 6.3 and 2.6 % for A3V3C3 and A3V1C3, respectively. This is attributable to the fact that vertical diffusion has a much higher temporal frequency than the other transport processes, especially near the surface.

When the flux limiter is switched off in the A3V1C3 case, RMSDs are increased globally (Fig. 2f). The region where the RMSD has most pronouncedly increased is the stratosphere. This is probably because the flux limiter no longer suppresses

15 the numerical oscillation near the top of the model domain, which is much larger than the CO_2 concentration variations in the stratosphere. But in the troposphere, the numerical oscillations are not so large compared to the CO_2 concentration variations. Consequently, the relative error is 7.5 % at the surface, which is larger than A3V1C3 but less than the 6-hourly vertical diffusion cases (A6V6C6, A3V6C6, A3V6C3), and 9.0 % at 300 hPa, which is the highest number in all the sensitivity tests (Table 2).

Figure 3 shows the annual mean difference of CO_2 concentration at the surface between the off-line and one-line models,

20 for A6V6C6, A3V3C3, A3V1C3 and A3V1C3 without the flux limiter. In fact, these differences represent biases from the on-line calculation induced by the data-thinning. Figure 3a shows that even the lowest temporal resolution of 6-hourly data input (A6V6C6) reproduces well the CO_2 concentrations over the oceans, where the bias is quite small (< 0.2 ppm). Meanwhile over the terrestrial areas, we see significantly large biases. Specifically, they are more than 4 ppm over the tropical regions of Amazon and Africa; these values are all negative due to the systematic underestimation of CO_2 accumulation during nighttime.

25 Furthermore, since the results of A3V6C6 and A3V6C3 are very similar to that of A6V6C6, the resolution of the vertical diffusion coefficient data is a major factor contributing to the data-thinning error, particularly over the terrestrial biosphere in the summertime when strong diurnal variations exist. These biases are reduced but still larger than 1 ppm even by halving the temporal interval (A3V3C3; Fig. 3b). However, by increasing the temporal resolution of the vertical diffusion coefficient data to hourly, the biases become nearly indiscernible (A3V1C3; Fig. 3c). Since we still use the moderate resolution of 3-hourly time

30 step for the advection and cumulus convection processes, the necessary disk storage of A3V1C3 for 1 year is not significantly large (approximately 50 GB, after partly performing a 2-byte data compression). Therefore, we set the A3V1C3 configuration to be the default for the glevel-5 simulations. When the flux limiter is switched off in A3V1C3, the bias increases slightly over the terrestrial areas but mostly less than 1 ppm (Fig. 3d). This bias is relatively small compared to the RMSD shown in Fig. 2f. Therefore, A3V1C3 without the flux limiter would be permissible, only if the focus is on the concentration in the troposphere.

This model configuration should be used when the model linearity is stringently required, such as in the use with the discrete adjoint.

3.3 Comparison with observations

In order to assess the magnitude of the off-line model error, we compare the simulated CO_2 concentrations with the observed measurements at Minamitorishima, located in the western North Pacific (Wada et al., 2011), and at Karasevoe, located in West Siberia (Sasakawa et al., 2010), as well as with the continuous aircraft CONTRAIL (Comprehensive Observation Network for Trace gases by Airliner: Machida et al., 2008) measurements obtained at 8-10 km altitude over Narita, Japan (each observation location is shown in Fig. 3a), representing marine background, continental, and upper-troposphere conditions, respectively. Figure 4 shows the observed and simulated CO_2 concentrations at each site. Generally, the on-line model reproduces relatively well the observed CO_2 concentration variations, partly due to the inversion flux we use. In the inversion, we use the Minamitorishima and CONTRAIL data to constrain the flux optimization (Niwa et al., 2012). But the high reproducibility of the synoptic variations indicates a reasonable transport performance of NICAM-TM, given the fact that we use monthly mean observations in the inversion. The RMSD value between the observation and the model is quite small; 0.92 and 1.36 ppm at Minamitorishima and over Narita, respectively. Meanwhile the RMSD at Karasevoe, whose observation is independent of the inversion, is 5.72 ppm. Compared to those RMSDs, the RMSD between the off-line and on-line models is negligibly small, even for the lowest resolution of A6V6C6 except at Karasevoe (Fig. 4). At Karasevoe, the meteorological resolution of A6V6C6 results in the RMSD value of 2.93 ppm. As shown in Fig. 4b, the off-line model produces lower CO_2 values compared to those produced by the on-line model during the summer, whose magnitude is comparable to the difference between the on-line model and the observation. As stated earlier, this is likely due to the underestimation of CO_2 accumulation during the nighttime and is the cause of the negative bias shown in Fig. 3a. By increasing the temporal resolution of the vertical diffusion coefficient to hourly (A3V1C3), we obtain a sufficiently small RMSD value of 0.24 ppm. Even without the flux limiter, the RMSD is modestly small (0.86 ppm) and the difference does not have any distinct positive or negative tendency (Fig. 4b).

3.4 Validation of the adjoint model

We now validate the exactitude of the adjoint model using the reciprocity property with its corresponding forward models. Detail description of the reciprocity property can be found in the literature (Hourdin and Talagrand, 2006; Hourdin et al., 2006; Haines et al., 2014; Wilson et al., 2014). In Eq. (6), if $\mathbf{x}$ and $\mathbf{y}$ are the basis unit vectors having 1 for ith and jth elements respectively and 0 for all the others (i.e. $\mathbf{x} = (0\cdots0,1,0\cdots0)^T$ and $\mathbf{y} = (0\cdots0,1,0\cdots0)^T$), a value sampled at j, which is simulated from $\mathbf{x}$ with the forward model $((\mathbf{Mx})^T\mathbf{y} = (\mathbf{Mx})_j = M_{j,i})$, should coincide with the value simulated from y with the adjoint model and subsequently sampled at i (xT(MTy)=(MTy)i=Mj,i). Checking this reciprocity, we can verify the exactitude of the adjoint method. To evaluate the reciprocity for both the discrete and continuous adjoint models, we use the forward model without and with the flux limiter, respectively. The former forward/adjoint model set is linear but does not ensure monotonicity, while the latter set is nonlinear but ensures monotonicity. Both in the forward and adjoint model simulations, we use the configuration of A3V1C3 for the meteorological input.

For a case study, we examine an Asian outflow event, which is a typical transport phenomenon in East Asia during the winter–spring season (e.g. Sawa et al., 2007). We prescribe a surface flux at the model grid (X) located on the coast of East Asia representing the basis unit vector **x** (its location is denoted by the cyan open circle in Fig. 5b). Meanwhile, we prepare 160 observational basis unit vectors (**y**), whose sampling points are regularly located at 3 km altitude over an area enclosed

5 by 14–32°N and 111–159°E (denoted by cyan dots in Fig. 5a). The simulation period is 7 days starting on 1 January 2010. The flux is time invariant; that is, the vector **x** is a function of space only. Figure 5a shows the concentration field at the end of the period, as simulated by the forward model with the flux limiter. On the other hand, Fig. 5b shows the sensitivities of the observation Y that is located at the eastern edge of the range (denoted by the cyan triangle in Fig. 5a) against the surface fluxes (i.e. footprint). This sensitivity is calculated by the continuous adjoint. We find that, using the discrete adjoint, the calculated

10 footprint pattern is quite similar to that shown in Fig. 5b; this is not surprising since the forward simulation without the flux limiter does not introduce substantial errors in the troposphere, as previously shown. As the concentration field shown Fig. 5a is simulated from the unit flux, it also represents the degree of spatial sensitivity between the flux and the observation. According to Eq. (6), the concentration value sampled at the observation point Y should coincide with the footprint value located at the flux point X. Performing adjoint simulations for the remaining 159 observation points, we can evaluate the overall reciprocity

15 of the adjoint model.

Figure 6 shows a scatter diagram of the 160 pairs of forward concentration values at the observation points with their corresponding adjoint footprint values at the flux point X. It can be seen in the figure that the footprint values simulated by the discrete adjoint show a near complete one-to-one correspondence with the corresponding concentration values to within the computer machine accuracy. This demonstrates that the discrete adjoint has the exact reciprocity against the forward model

20 without the flux limiter. On the other hand, the continuous adjoint does not have the exact reciprocity but it is reasonably approximated. Figure 6 also demonstrates that the continuous adjoint successfully avoids negative sensitivities because of the flux limiter, while the discrete adjoint calculation does produce negative sensitivities.

3.5 Adjoint trajectory analysis

Finally, we apply the adjoint sensitivities to a transport trajectory analysis. Generally, the adjoint model provides sensitivities

25 of a specified scalar value with respect to concentrations and surface fluxes (Appendix A). When the scalar value is set to an observed concentration, the cost functional is defined a

$$J = \int\limits_{t}^{t_o} \int\limits_{\Omega} g(q) d\Omega dt', \tag{9}$$

$$g(q) = q(x,t')\delta(x - x_o)\delta(t' - t_o), \tag{10}$$

where δ is the delta function and x_o and t_o represent the observed location and time respectively; therefore, the value of the cost

30 functional corresponds to the observed concentration $q(x_o, t_o)$. According to Appendix A, the change of the cost functional is

given by

$$\Delta J = \Delta q(x_o, t_o) = \int_t^{t_o} \int_\Omega \left(\mathcal{F}^* q^*(x, t')\right) \Delta s(x, t') d\omega dt' + \int_\Omega q^*(x, t) \Delta q(x, t) d\omega, \tag{11}$$

where $\mathcal{F}^*$ represents the adjoint of the transferring operator from flux to concentration, and Δs denotes the flux perturbation. $\mathcal{F}^* q^*$ and q^* denote the sensitivities of the observed concentration with respect to the surface flux and concentration, respec-

5 tively. If considered processes are all linear (which is the case in this study since we consider only atmospheric transport), we can omit Δ. Then, the first and second terms represent respectively the actual contributions of the surface flux from t to t_o and the concentration at t to the observed concentration. For our analysis, we investigate the spatial structures of these sensitivity quantities normalized by $q(x_o, t_o)$, i.e. $\int_t^{t_o} \left(\mathcal{F}^* q^*(x, t')\right) s(x, t') dt' / q(x_o, t_o)$ and $q^*(x, t) q(x, t) / q(x_o, t_o)$. These quantities derived by the adjoint model have been utilized in previous studies for diagnosing trace gas transport in the atmosphere (Vukićević

10 and Hess, 2000; Hess and Vukicevic, 2003) and a pathway of a waterer mass in the ocean (Fujii et al., 2013).

Using such adjoint-derived quantities, we analyze three high CO_2 concentration events; they were observed at Minamitorishima on 24 January, at Karasevoe on 27 December, and at 8 km over Narita on 12 January in 2010 (denoted by the cyan arrows in Fig. 4). These high-concentration events are chosen for relatively good model reproducibility. Figure 7 shows the normalized flux contribution and "adjoint trajectory volumes" (Hess and Vukicevic, 2003) against each event. The adjoint tra-

15 jectory volume is derived by averaging $q^*(x, t) q(x, t) / q(x_o, t_o)$ for each day previous to the observation time. Overlaying the averaged $q^*(x, t) q(x, t) / q(x_o, t_o)$ shows the pathway of the air mass that caused each of the high CO_2 events at the observation location and time. This analysis approach resembles the one taken by Hess and Vukicevic (2003). The forward simulation that calculates $q(x, t)$ and the adjoint simulation that calculates $q^*(x, t)$ and $\mathcal{F}^* q^*(x, t)$ are performed for one week period previous to each observation time. Here, we show the results calculated by the continuous adjoint model, taking the advantage of its

20 monotonicity property. However, the discrete adjoint model also produces similar sensitivity features (not shown).

Interestingly, the analysis indicates that three high concentration events were produced differently from each other. The flux contribution shows that the event observed at Minamitorishima originated from the Korean Peninsula and eastern China (Fig. 7a). Furthermore, the sharp adjoint trajectory volume indicates that the transport of the high CO_2 plume was characterized by slow diffusion. For the event observed at Karasevoe, the analysis indicates that the air mass that produced the high CO_2

25 concentration was advected from the west, but fluxes in the vicinity of the observation site contributed to the observed concentration (Fig. 7b). This local flux contribution is a result of a very thin mixed layer, as indicated by the vertical structure of the trajectory volume that is concentrated below 1km. Figure 7c shows that the high concentration event observed over Narita originated from southeast China. The adjoint trajectory volume indicates that the horizontal transport of the air mass from China to Japan was fast (taking only about 2 days) compared to the other cases because of the strong westerlies in the free

30 troposphere. Before this fast eastward transport, the analysis also indicates the possibility of an air mass propagation westward along the slope of the topography. Therefore, this result suggests that the topographical uplifting may have a significant role in high CO_2 concentration events frequently observed over Narita (Shirai et al., 2012).

4 Conclusions

We have developed forward and adjoint models based on NICAM-TM, as part of the 4D-Var system for atmospheric GHGs inversions. Both of these models are off-line. Therefore, the models are computationally efficient enough to make the 4D-Var iterative calculation feasible. The computational cost of the off-line forward model is about ten times less than that of the corresponding on-line model calculation. Furthermore, the adjoint model computational cost is nearly the same as that of the forward model.

The archived meteorological data used in the forward and adjoint models are prepared by the on-line AGCM calculation of NICAM in advance. In this study, we have developed the capability of variable temporal resolution of individual meteorological transport data, to minimize the off-line model errors owing to the data thinning. Through sensitivity tests using CO_2 as a tracer, we have determined that the temporal resolution of the vertical diffusion coefficient should be high, otherwise a significantly large systematic bias is introduced near the surface due to the underestimation of CO_2 accumulation during the nighttime. For the spatial resolution used in this study (the horizontal grid interval is approximately 240 km), the use of 1-hour interval for the vertical diffusion coefficient, while 3-hour interval for the others (A3V1C3), is enough to simulate CO_2 concentrations that are reasonably consistent with those produced by on-line calculation. By comparing with the observations, we have found that the error from the data thinning in A3V1C3 is negligible compared with the intrinsic model performance. In a case without using the flux limiter, we have found significantly large errors in the stratosphere, while the errors in the troposphere were less so and tolerable. Therefore, simulations without the flux limiter can be carried out in studies focused only on the troposphere.

For the adjoint model, we have explored the relative impact of using discrete adjoint or continuous adjoint on the advective transport process. Using an Asian outflow case, we have demonstrated perfect adjoint relationship of the discrete adjoint with its corresponding forward model in which the flux limiter is turned off. In the same analysis, the continuous adjoint has also shown reasonable adjoint exactitude against the forward model with the flux limiter turned on. Furthermore, we have found that the adjoint model can be used in attribution studies in which surface flux contributions are diagnosed as a function of air mass pathway when interpreting observed high CO_2 concentration events.

Based on the results of this study, we have developed a new 4D-Var system for performing CO_2 inversions. Application of the 4D-Var system and its results are described in the accompanying paper by Niwa et al. (2016). In the accompanying paper, the A3V1C3 configuration is used to judge which of the adjoint calculation methods, discrete or continuous, is better relative to the quality of produced inversion results.

The icosahedral grid model such as NICAM is a new type of model and is becoming popular in dynamical meteorology research fields as remarkable innovations in supercomputers are made. However, there are still only a few studies of its applications in atmospheric chemistry and inversion/assimilation calculations (e.g. Elbern et al., 2010). One prominent feature of the NICAM-TM 4D-Var system is the perfect mass conservation, as described in Section 2.1. Another advantage of the system is its computational efficiency when applied to linear GHG inversion problems. If we limit the analysis period to a short time, a global high-resolution inversion would be feasible as long as sufficient data storage capacity is available. Furthermore, regional high-resolution inversion would also be possible with the grid stretching technique (Tomita, 2008; Goto et al., 2015).

It is expected that the system developed in this study and the accompanying paper would exploit new observations and open up new avenues for GHG inversions.

Code availability

Development of NICAM-TM is being continued by the authors. The source codes of NICAM-TM are available for those
5 who are interested. The source codes of NICAM-TM are included in the package of the parent model NICAM, which can be obtained upon request under the general terms and conditions (http://nicam.jp/hiki/?Research+Collaborations).

Appendix A: Adjoint sensitivity

Here we explain the theory of the adjoint sensitivity following the description of Vukićević and Hess (2000). The tracer transport equation can be written in the following compact form of

$$\mathcal{L}q = \mathcal{F}s, \tag{A1}$$

where $\mathcal{L}$ is the transport operator,

$$\mathcal{L} \equiv \frac{\partial}{\partial t} + \mathcal{A} + \mathcal{V} + \mathcal{C}. \tag{A2}$$

The operator $\mathcal{F}$ is transferring surface flux s to concentration, and the operators for advection, vertical diffusion and cumulus convection are represented as $\mathcal{A}$, $\mathcal{V}$, and $\mathcal{C}$, respectively. Then, the adjoint operator $\mathcal{L}^*$ is defined as

$$\mathcal{L}^* \equiv -\frac{\partial}{\partial t} + (\mathcal{A}^* + \mathcal{V}^* + \mathcal{C}^*), \tag{A3}$$

where $\mathcal{A}^*$, $\mathcal{V}^*$, and $\mathcal{C}^*$ are the adjoint operators for $\mathcal{A}$, $\mathcal{V}$, and $\mathcal{C}$.

We characterize the solution of the tracer transport equation (A1) by the cost functional J as

$$J = \int_{t_1}^{t_2} \int_{\Omega} g(q) d\omega dt, \tag{A4}$$

where $[t_1, t_2]$ is the time interval examined, Ω is the spatial domain, $d\omega$ is the area differential, and $g(q)$ is the diagnostic
20 operator of q. Then the change by the perturbation of q is described as

$$\Delta J = \int_{t_1}^{t_2} \int_{\Omega} \frac{\partial g}{\partial q} \Delta q \, d\omega dt. \tag{A5}$$

The adjoint operator $\mathcal{L}^*$ defines an adjoint equation for the adjoint variable q^* as

$$\mathcal{L}^* q^* = \frac{\partial g}{\partial q}. \tag{A6}$$

Multiplying Eq. (A6) by Δq, and integrating over time and over the spatial domain, we obtain

$$\Delta J = \int\limits_{t_1}^{t_2} \int\limits_{\Omega} (\mathcal{L}^* q^*)\, \Delta q\; d\omega dt. \tag{A7}$$

By integration by parts, Eq. (A7) transforms to

$$\Delta J = \int\limits_{t_1}^{t_2} \int\limits_{\Omega} q^* (\mathcal{L}\Delta q)\, d\omega dt - \int\limits_{\Omega} [q^* \Delta q]_{t_1}^{t_2}\, d\omega - \int\limits_{t_1}^{t_2} [q^* \Delta q]_{O(\omega)}\, dt, \tag{A8}$$

5   where $O(\omega)$ denotes the boundary of the integration domain. Using Eq. (A1) and the adjoint operator $\mathcal{F}^*$ for $\mathcal{F}$, and specifying $q^* = 0$ at $t = t_2$ and $O(\omega)$ (no inflow/outflow of q^* at the boundary), we finally obtain

$$\Delta J = \int\limits_{t_1}^{t_2} \int\limits_{\Omega} (\mathcal{F}^* q^*(x,t))\, \Delta s(x,t) d\omega dt - \int\limits_{\Omega} q^*(x,t_1) \Delta q(x,t_1) d\omega. \tag{A9}$$

In Eq. (A9), $\mathcal{F}^* q^*(x,t)$ and $q^*(x,t_1)$ represent the sensitivities of ΔJ against the flux change ($\Delta s(x,t)$) and the change of the concentration at t_1 ($\Delta q(x,t_1)$), which are generally called adjoint sensitivities. If the cost functional J represents an observed

10   quantity, then $\int_{t_1}^{t_2} \mathcal{F}^* q^*(x,t) dt$ expresses its footprint as shown in Fig. 5b.

Acknowledgements. We thank Kaz Higuchi of York University, Canada, for his fruitful comments on the manuscript. The Minamitorishima CO_2 observational data are downloaded from the World Data Centre for Greenhouse Gases (WDCGG). We would like to acknowledge the staff of Japan Meteorological Agency for providing the data via the WDCGG site. This study is supported mainly by the Environment Research and Technology Development Fund (2-1401) of the Ministry of the Environment, Japan. This study is also supported partly by

15   the cooperative research for climate system of Atmosphere and Ocean Research Institute, the University of Tokyo, and by "advancement of meteorological and global environmental predictions utilizing observational 'Big Data'" of the social and scientific priority issues (Theme 4) to be tackled by using post K computer of the FLAGSHIP2020 Project. The calculations of this study were performed on the super computer system, FUJITSU PRIMEHPC FX100, of Meteorological Research Institute.

References

Andres, R. J., Boden, T., and Marland, G.: Monthly Fossil-Fuel CO_2 Emissions: Mass of Emissions Gridded by One Degree Latitude by One Degree Longitude, Carbon Dioxide Information Analysis Center, Oak Ridge National Laboratory, U.S. Department of Energy, Oak Ridge, Tenn., U.S.A., doi:10.3334/CDIAC/ffe.MonthlyMass.2013, 2013.

5 Arakawa, A. and Schubert, W. H.: Interaction of a cumulus cloud ensemble with the large-scale environment, Part I, J. Atmos. Sci., 31, 674–701, doi:10.1175/1520-0469(1974)031<0674:IOACCE>2.0.CO;2, 1974.

Baker, D. F., Doney, S. C., and Schimel, D. S.: Variational data assimilation for atmospheric CO_2, Tellus B, 58, 359–365, doi:10.1111/j.1600-0889.2006.00218.x, 2006.

Basu, S., Guerlet, S., Butz, A., Houweling, S., Hasekamp, O., Aben, I., Krummel, P., Steele, P., Langenfelds, R., Torn, M., Biraud, S.,
10 Stephens, B., Andrews, A., and Worthy, D.: Global CO_2 fluxes estimated from GOSAT retrievals of total column CO_2, Atoms. Chem. Phys., 13, 8695–8717, doi:10.5194/acp-13-8695-2013, 2013.

Bregman, B., Segers, A., Krol, M., Meijer, E., and Velthoven, P.: On the use of mass-conserving wind fields in chemistry-transport models, Atoms. Chem. Phys., 3, 447–457, doi:10.5194/acp-3-447-2003, 2003.

Chevallier, F., Fisher, M., Peylin, P., Serrar, S., Bousquet, P., Bréon, F.-M., Chédin, A., and Ciais, P.: Inferring CO_2 sources and sinks from
15 satellite observations: Method and application to TOVS data, J. Geophys. Res., 110, doi:10.1029/2005JD006390, d24309, 2005.

Chevallier, F., Ciais, P., Conway, T. J., Aalto, T., Anderson, B. E., Bousquet, P., Brunke, E. G., Ciattaglia, L., Esaki, Y., Fröhlich, M., Gomez, A., Gomez-Pelaez, A. J., Haszpra, L., Krummel, P. B., Langenfelds, R. L., Leuenberger, M., Machida, T., Maignan, F., Matsueda, H., Morguí, J. A., Mukai, H., Nakazawa, T., Peylin, P., Ramonet, M., Rivier, L., Sawa, Y., Schmidt, M., Steele, L. P., Vay, S. A., Vermeulen, A. T., Wofsy, S., and Worthy, D.: CO_2 surface fluxes at grid point scale estimated from a global 21 year reanalysis of atmospheric
20 measurements, J. Geophys. Res., 115, doi:10.1029/2010JD013887, 2010.

Chikira, M. and Sugiyama, M.: A Cumulus Parameterization with State-Dependent Entrainment Rate. Part I: Description and Sensitivity to Temperature and Humidity Profiles, J. Atmos. Sci., 67, 2171–2193, doi:10.1175/2010JAS3316.1, 2010.

Elbern, H., Schwinger, J., and Botchorishvili, R.: Chemical state estimation for the middle atmosphere by four-dimensional variational data assimilation: System configuration, J. Geophys. Res., 115, doi:10.1029/2009JD011953, 2010.

25 Errico, R.: What Is an Adjoint Model?, Bull. Amer. Meteor. Soc., 78, 2577–2591, doi:10.1175/1520-0477(1997)078<2577:WIAAM>2.0.CO;2, 1997.

Fujii, Y., Nakano, T., Usui, N., Matsumoto, S., Tsujino, H., and Kamachi, M.: Pathways of the North Pacific Intermediate Water identified through the tangent linear and adjoint models of an ocean general circulation model, J. Geophys. Res., 118, 2035–2051, doi:10.1002/jgrc.20094, 2013.

30 Godunov, S.: A difference scheme for numerical computation of discontinuous solutions of equations in fluid dynamics, Matematicheskii Sbornik, 47, 271–306, 1959.

Goto, D., Dai, T., Satoh, M., Tomita, H., Uchida, J., Misawa, S., Inoue, T., Tsuruta, H., Ueda, K., Ng, C., Takami, A., Sugimoto, N., Shimizu, A., Ohara, T., and Nakajima, T.: Application of a global nonhydrostatic model with a stretched-grid system to regional aerosol simulations around Japan, Geosci. Model Dev., 8, 235–259, doi:10.5194/gmd-8-235-2015, 2015.

35 Gou, T. and Sandu, A.: Continuous versus discrete advection adjoints in chemical data assimilation with CMAQ, Atmos. Environ., 45, 4868–4881, doi:10.1016/j.atmosenv.2011.06.015, 2011.

Gross, E. S., Bonaventura, L., and Rosatti, G.: Consistency with continuity in conservative advection schemes for free-surface models, Int. J. Numer. Meth. Fluids, 38, 307–327, 2002.

Haines, P., Esler, J., and Carver, G.: Technical Note: Adjoint formulation of the TOMCAT atmospheric transport scheme in the Eulerian backtracking framework (RETRO-TOM), Atoms. Chem. Phys., 14, 5477–5493, doi:10.5194/acp-14-5477-2014, 2014.

5   Hakami, A., Henze, D., Seinfeld, J., Singh, K., Sandu, A., Kim, S., Byun, D., and Li, Q.: The adjoint of CMAQ, Environ. Sci. Technol., 41, 7807–17, doi:10.1021/es070944p, 2007.

Heimann, M.: The Global Atmospheric Tracer Model TM2, Tech. Rep. 10, Max-Planck-Institut für Biogeochemie, Hamburg, Germany, 1995.

Heimann, M. and Keeling, C.: A three-dimensional model of atmospheric CO_2 transport based on obaserved winds: 2: Model description
10   and simulated tracer experiments, Geophys. Mon., 55, 237–275, 1989.

Hess, P. G. and Vukicevic, T.: Intercontinental transport, chemical transformations, and baroclinic systems, J. Geophys. Res., 208, doi:10.1029/2002JD002798, 2003.

Hourdin, F. and Talagrand, O.: Eulerian backtracking of atmospheric tracers. I: Adjoint derivation and parametrization of subgrid-scale transport, Quart. J. Roy. Meteor. Soc., 132, 567–583, doi:10.1256/qj.03.198.A, 2006.

15   Hourdin, F., Talagrand, O., and Idelkadi, A.: Eulerian backtracking of atmospheric tracers. II: Numerical aspects, Quart. J. Roy. Meteor. Soc., 132, 585–603, doi:10.1256/qj.03.198.B, 2006.

Huijnen, V., Williams, J., Weele, M., Noije, T., Krol, M., Dentener, F., Segers, A., Houweling, S., Peters, W., Laat, J., Boersma, F., Bergamaschi, P., Velthoven, P., Sager, P., Eskes, H., Alkemade, F., Scheele, R., Nédélec, P., and Pätz, H.: The global chemistry transport model TM5: description and evaluation of the tropospheric chemistry version 3.0, Geosci. Model Dev., 3, 445–473, doi:10.5194/gmd-3-445-
20   2010, 2010.

Jöckel, P., von Kuhlmann, R., Lawrence, M., Steil, B., Brenninkmeijer, C., Crutzen, P., Rasch, P., and Eaton, B.: On a fundamental problem in implementing flux-form advection schemes for tracer transport in 3-dimensional general circulation and chemistry transport models, Quart. J. Roy. Meteor. Soc., 127, 1035–1052, 2001.

Kawa, S., Erickson, D., Pawson, S., and Zhu, Z.: Global CO_2 transport simulations using meteorological data from the NASA data assimi-
25   lation system, J. Geophys. Res., 109, doi:10.1029/2004JD004554, 2004.

Kodama, C., Terai, M., Noda, A., Yamada, Y., Satoh, M., Seiki, T., Iga, S.-i., Yashiro, H., Tomita, H., and Minami, K.: Scalable rank-mapping algorithm for an icosahedral grid system on the massive parallel computer with a 3-D torus network, Parallel Comput., 40, 362–373, doi:10.1016/j.parco.2014.06.002, 2014.

Liu, J., Bowman, K., Lee, M., Henze, D., Bousserez, N., Brix, H., Collatz, G. J., Menemenlis, D., Ott, L., Pawson, S., Jones, D., and Nassar,
30   R.: Carbon monitoring system flux estimation and attribution: impact of ACOS-GOSAT XCO_2 sampling on the inference of terrestrial biospheric sources and sinks, Tellus B, 66, doi:10.3402/tellusb.v66.22486, 2014.

Machida, T., Matsueda, H., Sawa, Y., Nakagawa, Y., Hirotani, K., Kondo, N., Goto, K., Nakazawa, T., Ishikawa, K., and Ogawa, T.: Worldwide Measurements of Atmospheric CO_2 and Other Trace Gas Species Using Commercial Airlines, J. Atmos. Oceanic Technol., 25, 1744–1754, doi:10.1175/2008JTECHA1082.1, 2008.

35   Matsueda, H., Machida, T., Sawa, Y., and Niwa, Y.: Long-term change of CO_2 latitudinal distribution in the upper troposphere, Geophys. Res. Lett., 42, 2508–2514, doi:10.1002/2014GL062768, 2015.

Meirink, J. F., Bergamaschi, P., Frankenberg, C., d'Amelio, M. T. S., Dlugokencky, E. J., Gatti, L. V., Houweling, S., Miller, J. B., Röckmann, T., Villani, M. G., and Krol, M. C.: Four-dimensional variational data assimilation for inverse modeling of atmospheric methane emissions: Analysis of SCIAMACHY observation, J. Geophys. Res., 113, doi:10.1029/2007JD009740, 2008.

Mellor, G. L. and Yamada, T.: A Hierarchy of Turbulence Closure Models for Planetary Boundary Layers, J. Atmos. Sci., 31, 1791–1806, 1974.

Miura, H.: An Upwind-Biased Conservative Advection Scheme for Spherical Hexagonal–Pentagonal Grids, Mon Weather Rev, 135, 4038–4044, doi:10.1175/2007MWR2101.1, 2007.

Miura, H., Satoh, M., Nasuno, T., Noda, A. T., and Oouchi, K.: A Madden–Jullian Oscillation event simulated using a global cloud-resolving model, Science, 318, 1763–1765, 2007.

Miyakawa, T., Satoh, M., Miura, H., Tomita, H., Yashiro, H., Noda, A., Yamada, Y., Kodama, C., Kimoto, M., and Yoneyama, K.: Madden-Julian Oscillation prediction skill of a new-generation global model demonstrated using a supercomputer., Nat. Commun., 5, 3769, doi:10.1038/ncomms4769, 2014.

Miyamoto, Y., Kajikawa, Y., Yoshida, R., Yamaura, T., Yashiro, H., and Tomita, H.: Deep moist atmospheric convection in a subkilometer global simulation, Geophys. Res. Lett., 40, 4922–4926, doi:10.1002/grl.50944, 2013.

Nakanishi, M. and Niino, H.: An Improved Mellor–Yamada Level-3 Model with Condensation Physics: Its Design and Verification, Boundary Layer Meteorol., 112, 1–31, doi:10.1023/B:BOUN.0000020164.04146.98, 2004.

Niwa, Y., Patra, P. K., Sawa, Y., Machida, T., Matsueda, H., Belikov, D., Maki, T., Ikegami, M., Imasu, R., Maksyutov, S., Oda, T., Satoh, M., and Takigawa, M.: Three-dimensional variations of atmospheric CO_2: aircraft measurements and multi-transport model simulations, Atoms. Chem. Phys., 11, 13 359–13 375, doi:10.5194/acp-11-13359-2011, 2011a.

Niwa, Y., Tomita, H., Satoh, M., and Imasu, R.: A Three-Dimensional Icosahedral Grid Advection Scheme Preserving Monotonicity and Consistency with Continuity for Atmospheric Tracer Transport, J. Meteor. Soc. Japan, 89, 255–268, doi:10.2151/jmsj.2011-306, 2011b.

Niwa, Y., Machida, T., Sawa, Y., Matsueda, H., Schuck, T. J., Brenninkmeijer, C. A. M., Imasu, R., and Satoh, M.: Imposing strong constraints on tropical terrestrial CO_2 fluxes using passenger aircraft based measurements, J. Geophys. Res., 117, doi:10.1029/2012JD017474, 2012.

Niwa, Y., Fujii, Y., Sawa, Y., Iida, Y., Ito, A., Satoh, M., Imasu, R., Tsuboi, K., Matsueda, H., and Saigusa, N.: A 4D-Var inversion system based on an icosahedral grid model (NICAM-TM 4D-Var v1.0): 2. Optimization scheme and identical twin experiment of atmospheric CO_2 inversion, manuscript submitted for publication, 2016.

Noda, A. T., Oouchi, K., Satoh, M., Tomita, H., Iga, S.-i., and Tsushima, Y.: Importance of the subgrid-scale turbulent moist process: Cloud distribution in global cloud-resolving simulations, Atmos. Res., 96, 208–217, doi:10.1016/j.atmosres.2009.05.007, 2010.

Olsen, S. C. and Randerson, J. T.: Differences between surface and column atmospheric CO_2 and implications for carbon cycle research, J. Geophys. Res., 109, doi:10.1029/2003JD003968, 2004.

Onogi, K., Tsutsui, J., Koide, H., Sakamoto, M., Kobayashi, S., Hatsushika, H., Matsumoto, T., Yamazaki, N., Kamahori, H., Takahashi, K., Kadokura, S., Wada, K., Kato, K., Oyama, R., Ose, T., Mannoji, N., and Taira, R.: The JRA-25 Reanalysis, J. Meteor. Soc. Japan, 85, 369–432, doi:10.2151/jmsj.85.369, 2007.

Patra, P. K., Takigawa, M., Dutton, G. S., Uhse, K., Ishijima, K., Lintner, B. R., Miyazaki, K., and Elkins, J. W.: Transport mechanisms for synoptic, seasonal and interannual SF_6 variations and "age" of air in troposphere, Atoms. Chem. Phys., 9, 1209–1225, doi:10.5194/acp-9-1209-2009, 2009.

Patra, P. K., Houweling, S., Krol, M., Bousquet, P., Belikov, D., Bergmann, D., Bian, H., P, C., Chipperfield, M., Corbin, K., A, F., Fraser, A., Gloor, E., Hess, P., Ito, A., Kawa, S., Law, R., Loh, Z., Maksyutov, S., Meng, L., Palmer, P., Prinn, R., Rigby, M., Saito, R., and Wilson,

C.: TransCom model simulations of CH_4 and related species: linking transport, surface flux and chemical loss with CH4 variability in the troposphere and lower stratosphere, Atoms. Chem. Phys., 11, 12 813–12 837, doi:10.5194/acp-11-12813-2011, 2011.

Peylin, P., Law, R. M., Gurney, K. R., Chevallier, F., Jacobson, A. R., Maki, T., Niwa, Y., Patra, P. K., Peters, W., Rayner, P. J., Rödenbeck, C., van der Laan-Luijkx, I. T., and Zhang, X.: Global atmospheric carbon budget: results from an ensemble of atmospheric CO_2 inversions,
5   Biogeosciences, 10, 6699–6720, doi:10.5194/bg-10-6699-2013, 2013.

Randerson, J. T., Thompson, M. V., Conway, T. J., Fung, I. Y., and Field, C. B.: The contribution of terrestrial sources and sinks to trends in the seasonal cycle of atmospheric carbon dioxide, Global Biogeochem. Cycles, 11, 535–560, doi:10.1029/97GB02268, 1997.

Rödenbeck, C.: Estimating CO_2 sources and sinks from atmospheric mixing ratio measurements using a global inversion of atmospheric transport, Max-Planck-Institut für Biogeochemie: Technical Paper 6, 2005.

10   Sandu, A., Daescu, D. N., Carmichael, G. R., and Chai, T.: Adjoint sensitivity analysis of regional air quality models, J. Comput. Phys., 204, 222–252, doi:10.1016/j.jcp.2004.10.011, 2005.

Sasakawa, M., Shimoyama, K., Machida, T., Tsuda, N., Suto, H., Arshinov, M., Davydov, D., Fofonov, A., Krasnov, O., Saeki, T., Koyama, Y., and Maksyutov, S.: Continuous measurements of methane from a tower network over Siberia, Tellus B, 62, 403–416, doi:10.1111/j.1600-0889.2010.00494.x, 2010.

15   Satoh, M., Matsuno, T., Tomita, H., Miura, H., Nasuno, T., and Iga, S.: Nonhydrostatic icosahedral atmospheric model (NICAM) for global cloud resolving simulations, J. Comput. Phys., 227, 3486–3514, doi:10.1016/j.jcp.2007.02.006, 2008.

Satoh, M., Tomita, H., Yashiro, H., Miura, H., Kodama, C., Seiki, T., Noda, A. T., Yamada, Y., Goto, D., Sawada, M., Miyoshi, T., Niwa, Y., Hara, M., Ohno, T., Iga, S., Arakawa, T., Inoue, T., and Kubokawa, H.: The Non-hydrostatic Icosahedral Atmospheric Model: description and development, Progress in Earth and Planetary Science, 1, 1–32, doi:10.1186/s40645-014-0018-1, 2014.

20   Sawa, Y., Tanimoto, H., Yonemura, S., Matsueda, H., Wada, A., Taguchi, S., Hayasaka, T., Tsuruta, H., Tohjima, Y., Mukai, H., Kikuchi, N., Katagiri, S., and Tsuboi, K.: Widespread pollution events of carbon monoxide observed over the western North Pacific during the East Asian Regional Experiment (EAREX) 2005 campaign, J. Geophys. Res., 112, doi:10.1029/2006JD008055, 2007.

Sawa, Y., Machida, T., and Matsueda, H.: Seasonal variations of CO_2 near the tropopause observed by commercial aircraft, J. Geophys. Res., 113, doi:10.1029/2008JD010568, 2008.

25   Sawa, Y., Machida, T., Matsueda, H., Niwa, Y., Tsuboi, K., Murayama, S., Morimoto, S., and Aoki, S.: Seasonal changes of CO_2, CH_4, N_2O and SF_6 in the upper troposphere/lower stratosphere over the Eurasian continent observed by commercial airliner, Geophys. Res. Lett., 42, 2001–2008, doi:10.1002/2014GL062734, 2015.

Shirai, T., Machida, T., Matsueda, H., Sawa, Y., Niwa, Y., Maksyutov, S., and Higuchi, K.: Relative contribution of transport/surface flux to the seasonal vertical synoptic CO_2 variability in the troposphere over Narita, Tellus B, 64, doi:10.3402/tellusb.v64i0.19138, 2012.

30   Stohl, A., Cooper, O. R., and James, P.: A Cautionary Note on the Use of Meteorological Analysis Fields for Quantifying Atmospheric Mixing, J. Atmos. Sci., 61, 1446–1453, doi:10.1175/1520-0469(2004)061<1446:ACNOTU>2.0.CO;2, 2004.

Stuhne, G. and Peltier, W.: Vortex Erosion and Amalgamation in a New Model of Large Scale Flow on the Sphere, J. Comput. Phys., 128, 58–81, doi:10.1006/jcph.1996.0196, 1996.

Takahashi, T., Sutherland, S. C., Wanninkhof, R., Sweeney, C., Feely, R. A., Chipman, D. W., Hales, B., Friederich, G., Chavez, F., Sabine, C.,
35   Watson, A., Bakker, D. C., Schuster, U., Metzl, N., Yoshikawa-Inoue, H., Ishii, M., Midorikawa, T., Nojiri, Y., Körtzinger, A., Steinhoff, T., Hoppema, M., Olafsson, J., Arnarson, T. S., Tilbrook, B., Johannessen, T., Olsen, A., Bellerby, R., Wong, C., Delille, B., Bates, N., and de Baar, H. J.: Climatological mean and decadal change in surface ocean pCO_2, and net sea-air CO_2 flux over the global oceans, Deep-Sea Research, Part II, 56, 554–577, 2009.

Thuburn, J.: Multidimensional Flux-Limited Advection Schemes, J. Comput. Phys., 123, 74–83, doi:10.1006/jcph.1996.0006, 1996.

Thuburn, J. and Haine, T. W. N.: Adjoints of Nonoscillatory Advection Schemes, J. Comput. Phys., 171, 616–631, doi:10.1006/jcph.2001.6799, 2001.

Tomita, H.: A Stretched Icosahedral Grid by a New Grid Transformation, J. Meteor. Soc. Japan, 86A, 107–119, doi:10.2151/jmsj.86A.107, 2008.

Tomita, H. and Satoh, M.: A new dynamical framework of nonhydrostatic global model using the icosahedral grid, Fluid Dyn. Res., 34, 357–400, doi:10.1016/j.fluiddyn.2004.03.003, 2004.

Tomita, H., Goto, K., and Satoh, M.: A New Approach to Atmospheric General Circulation Model: Global Cloud Resolving Model NICAM and its Computational Performance, Siam. J. Sci. Comput., 30, 2755–2776, doi:10.1137/070692273, 2008.

van der Werf, G. R., Randerson, J. T., Giglio, L., Collatz, G. J., Mu, M., Kasibhatla, P. S., Morton, D. C., DeFries, R. S., Jin, Y., and van Leeuwen, T. T.: Global fire emissions and the contribution of deforestation, savanna, forest, agricultural, and peat fires (1997–2009), Atoms. Chem. Phys., 10, 11 707–11 735, doi:10.5194/acp-10-11707-2010, 2010.

Vukićević, T. and Hess, P.: Analysis of tropospheric transport in the Pacific Basin using the adjoint technique, J. Geophys. Res., 105, 7213–7230, doi:10.1029/1999JD901110, 2000.

Vukićević, T., Steyskal, M., and Hecht, M.: Properties of Advection Algorithms in the Context of Variational Data Assimilation, Mon. Wea. Rev., 129, 1221–1231, doi:10.1175/1520-0493(2001)129<1221:POAAIT>2.0.CO;2, 2001.

Wada, A., Matsueda, H., Sawa, Y., Tsuboi, K., and Okubo, S.: Seasonal variation of enhancement ratios of trace gases observed over 10 years in the western North Pacific, Atmos. Environ., 45, 2129–2137, doi:10.1016/j.atmosenv.2011.01.043, 2011.

Wilson, C., Chipperfield, M., Gloor, M., and Chevallier, F.: Development of a variational flux inversion system (INVICAT v1.0) using the TOMCAT chemical transport model, Geosci. Model Dev., 7, 2485–2500, doi:10.5194/gmd-7-2485-2014, 2014.

Yokota, T., Yoshida, Y., Eguchi, N., Ota, Y., Tanaka, T., Watanabe, H., and Maksyutov, S.: Global Concentrations of CO_2 and CH_4 Retrieved from GOSAT: First Preliminary Results, SOLA, 5, 160–163, doi:10.2151/sola.2009-041, 2009.

Yumimoto, K. and Takemura, T.: The SPRINTARS version 3.80/4D-Var data assimilation system: development and inversion experiments based on the observing system simulation experiment framework, Geosci. Model Dev., 6, 2005–2022, doi:10.5194/gmd-6-2005-2013, 2013.

Table 1. Meteorological parameters used for the off-line forward and adjoint models

Parameter	Symbol	Time type	Related process
Air mass density	ρ	Snapshot	Advection
Air mass flux	$\mathbf{V}\,(=\rho\mathbf{v})$	Averaged	Advection
Vertical diffusion coefficient	K_v	Snapshot	Vertical diffusion
Water substances	q_w	Snapshot	Cumulus convection
Temperature	T	Snapshot	Cumulus convection
Cumulus base mass flux	M_B	Snapshot	Cumulus convection

Table 2. Temporal intervals for advection, vertical diffusion, and cumulus convection processes in each sensitivity test and relative errors globally averaged at the surface and 300 hPa. The relative error is calculated at each model grid by dividing RMSD by the standard deviation of the CO_2 concentration variation simulated by the on-line model for 2010.

Notation	Temporal interval [hour]			Relative error [%]	
	Advection	Vertical diffusion	Cumulus convection	Surface	300 hPa
A6V6C6	6	6	6	12.9	5.3
A3V6C6	3	6	6	12.7	4.8
A3V6C3	3	6	3	12.6	3.3
A3V3C3	3	3	3	6.3	2.2
A3V1C3	3	1	3	2.6	2.0
A3V1C3 w/o flux limiter	3	1	3	7.5	9.0
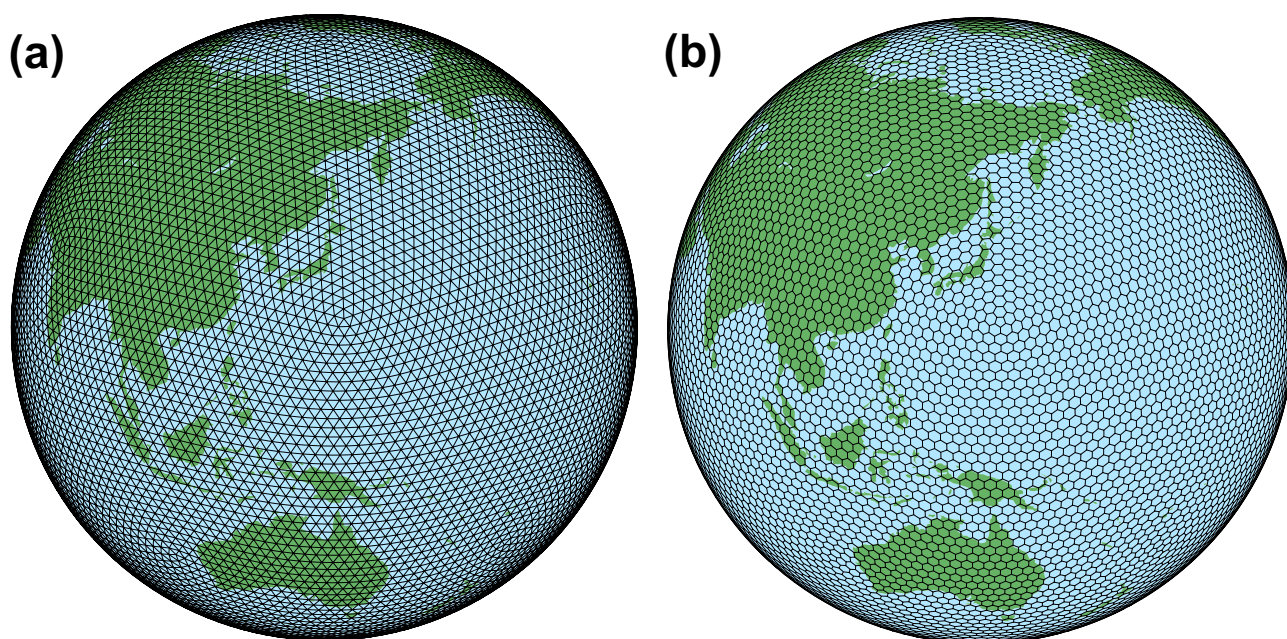
Figure 1. The grid distribution of NICAM glevel-5. Triangular elements produced from an icosahedron by five-times division (a) and control volumes constructed by connecting the mass centers of the triangular elements (b).
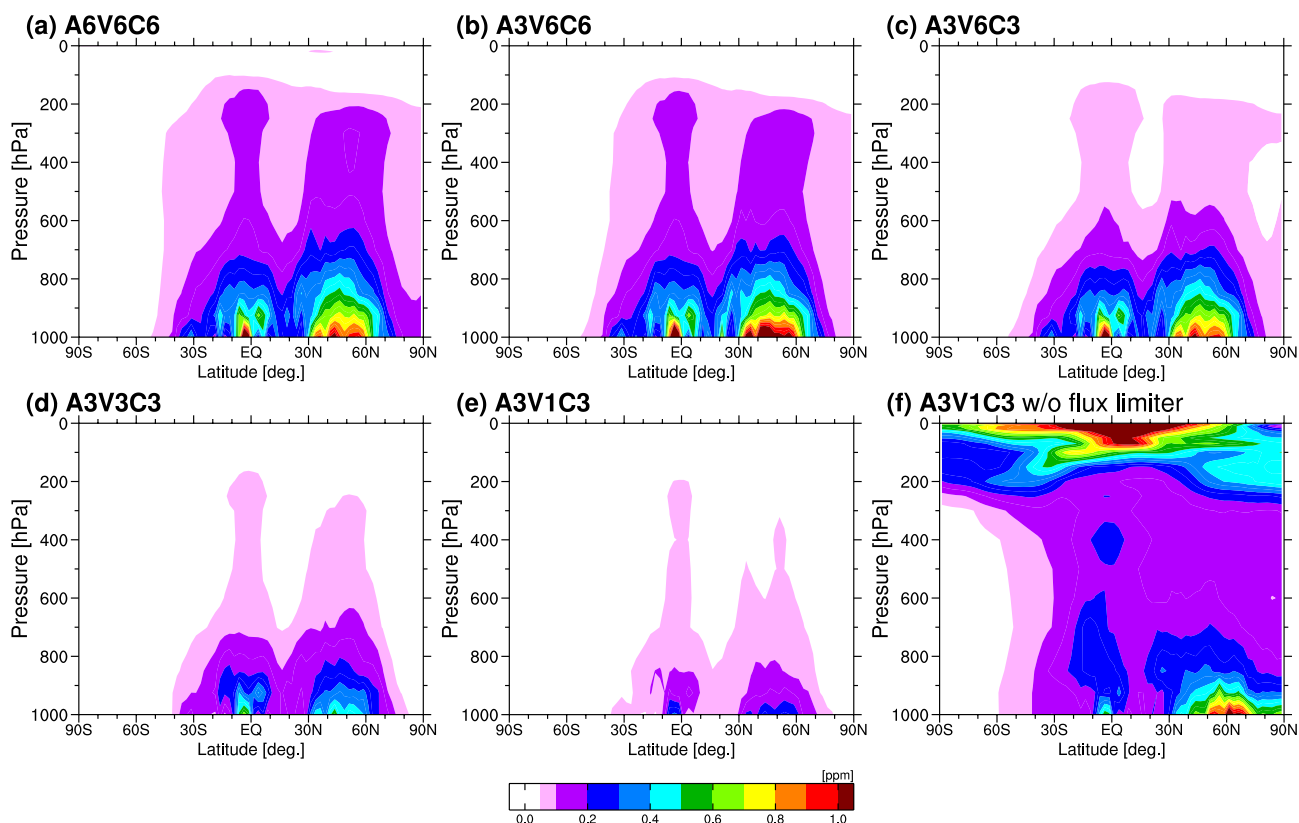
Figure 2. Zonal-mean latitude-pressure cross-section of root-mean-square difference (RMSD) of CO_2 concentration simulated by the off-line model against the on-line model. Time interval of the meteorological driver data is changed for each transport process as shown in Table 2 (a-e) and the same time resolutions are used as (e) but with the flux limiter switched off (f).
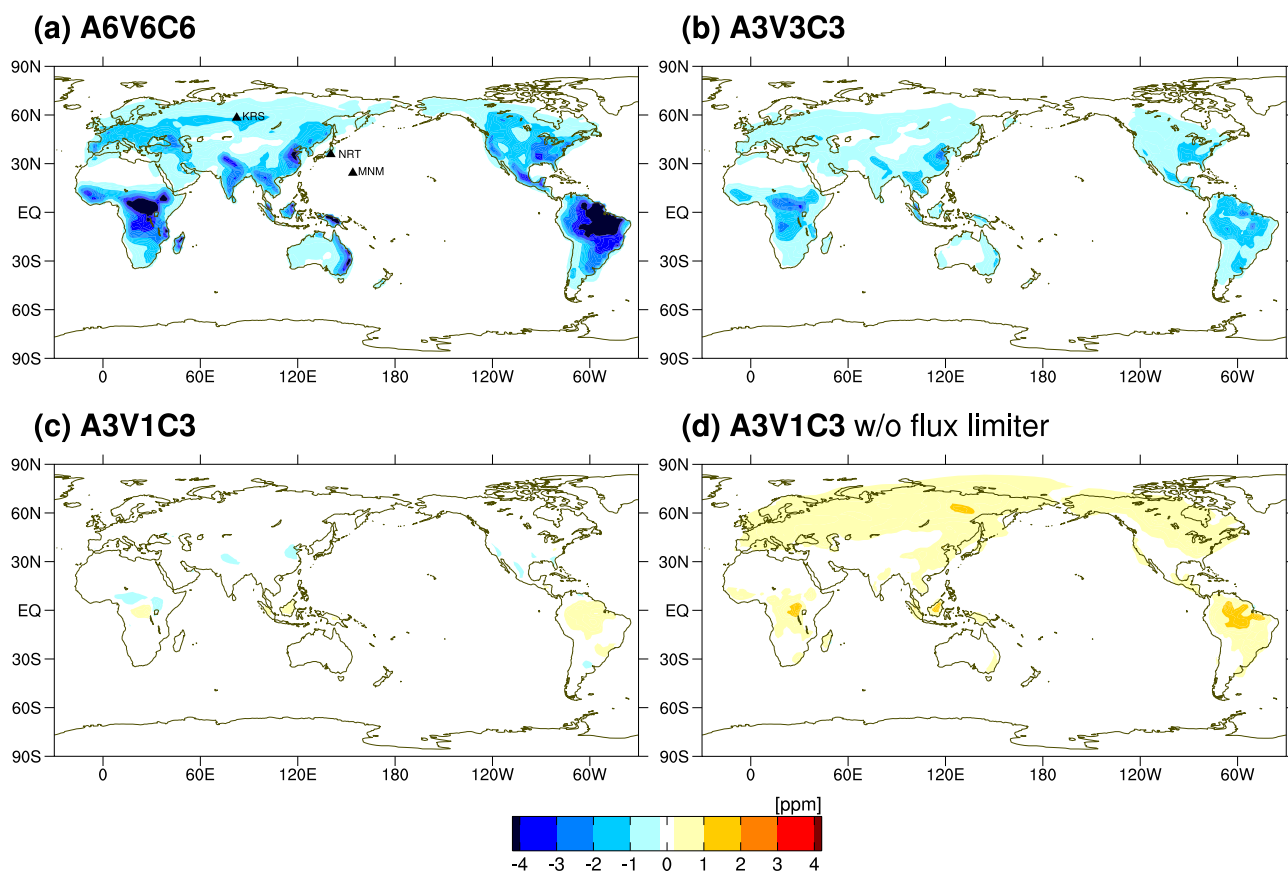
Figure 3. Annual mean difference of CO_2 concentration at the surface model layer between the off-line and on-line models (off-line minus on-line) for each sensitivity test: A6V6C6 (a), A3V3C3 (b), A3V1C3 (c) and A3V1C3 without the flux limiter (d). White colored areas signify absolute values less than 0.2 ppm. The geographical locations of Minamitorishima (MNM), Karasevoe (KRS), and Narita (NRT) are also indicated in (a).
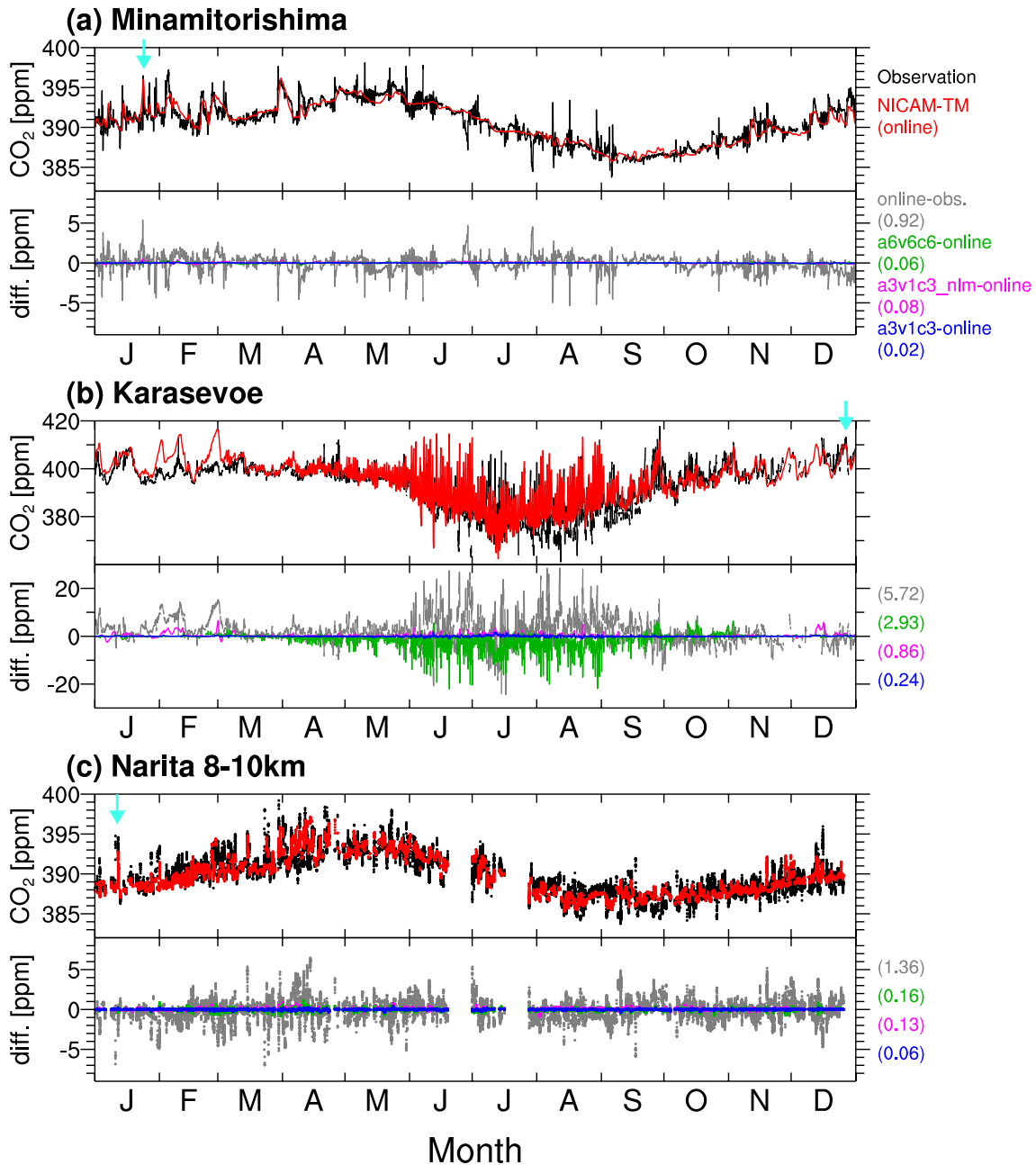
Figure 4. Time series of CO_2 concentration for 2010 at Minamitorishima (a), Karasevoe (b), and 8-10 km altitude over Narita (c). Each upper panel shows the time series observed (black) and simulated by the on-line model (red). Each lower panel shows differences of CO_2 concentrations between the on-line model and the observation (gray) and between the off-line model (green for A6V6C6, magenta for A3V1C3, blue for A3V1C3 without the flux limiter) and the on-line model. The number in the parenthesis gives the RMSD value for each sensitivity case. Note that only tropospheric data (determined by the dynamical tropopause (Sawa et al., 2008)) are used for the comparison over Narita.
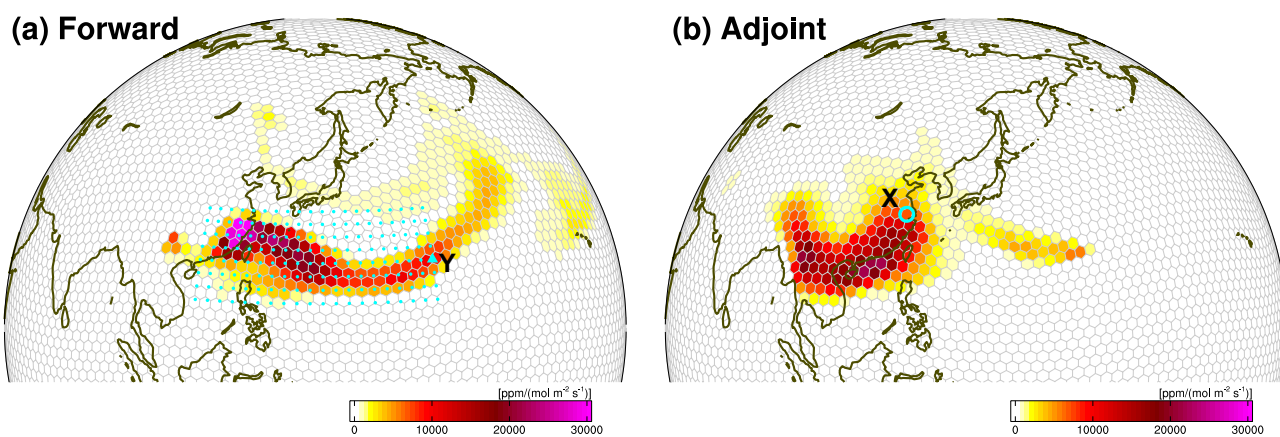
Figure 5. The concentration field at 3 km altitude on 0 UTC 8 January 2010 simulated by the forward model (with the flux limiter) from the basis unit flux X (a) and the sensitivities of the observation Y against the surface fluxes (footprint) simulated by the continuous adjoint model (b). The observation points, from which the adjoint sensitivities are calculated, are denoted as cyan dots and the location of observation Y is indicated by the cyan triangle (a). The location of the basis unit flux X is indicated by the cyan open circle (b).
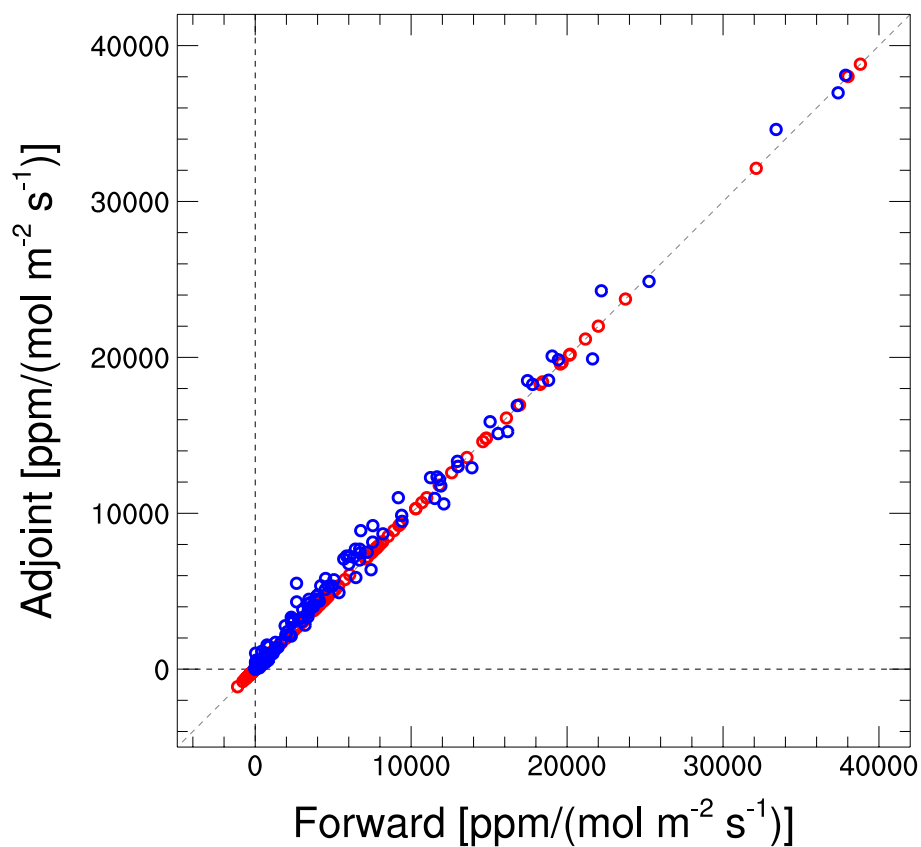
Figure 6. The scatter diagram showing 160 concentration values simulated by the forward model at the observation points versus their corresponding adjoint footprint values at the flux point X. The red open circles denote values from the linear model setup (the forward model without the flux limiter and the discrete adjoint model), while the blue open circles denote values from the nonlinear model setup (the forward model with the flux limiter and the continuous adjoint model).
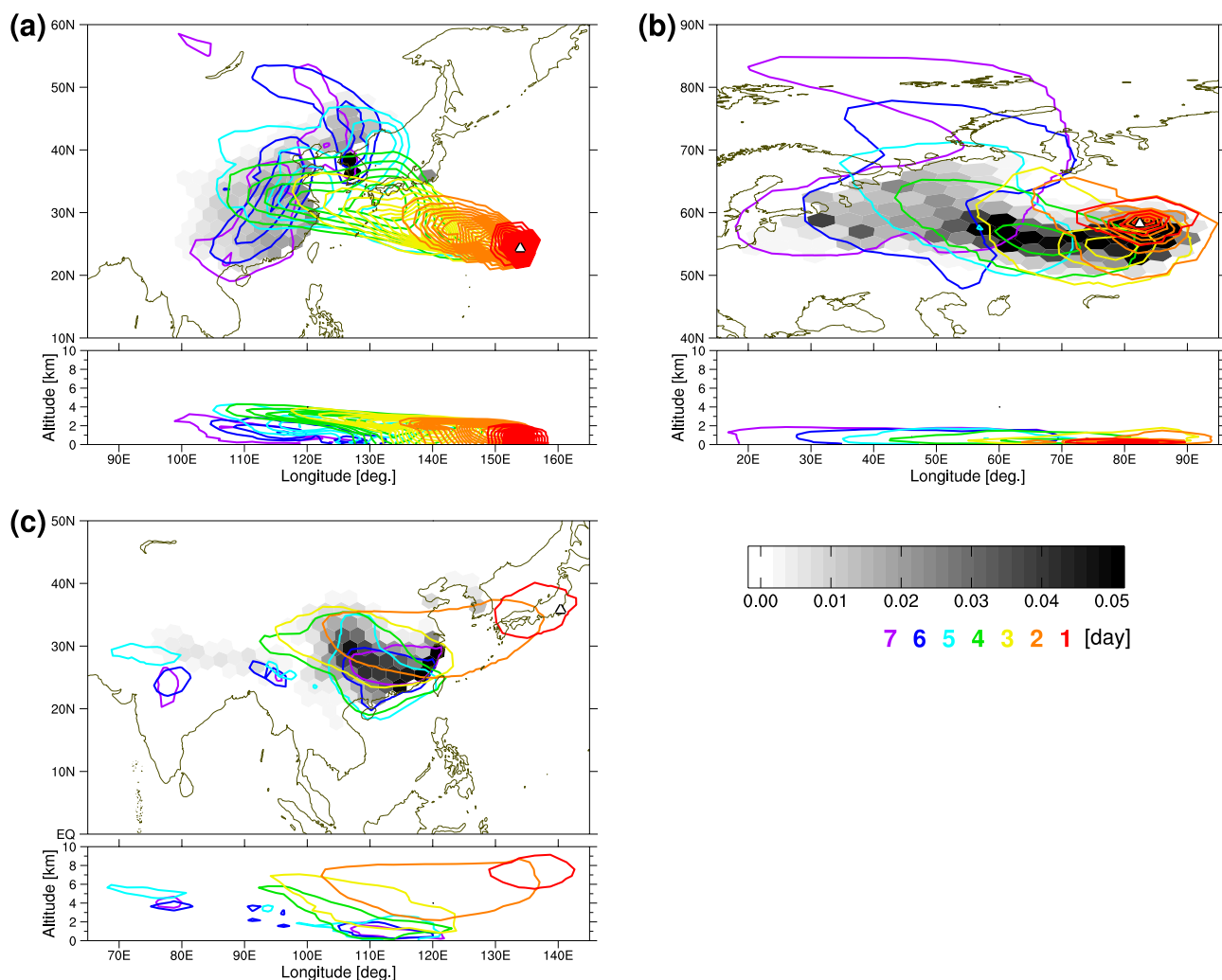
Figure 7. The normalized flux contributions (gray shades) and the adjoint trajectory volumes (color contours) for the high CO_2 concentration events observed at Minamitorishima on 24 January (a), at Karasevoe on 27 December (b), and at 8 km over Narita on 12 January in 2010 (c), which are denoted by the cyan arrows in Fig. 4. See the text for the definitions of the flux contribution and the adjoint trajectory volume. Each upper and lower panels present the horizontal and vertical structures of the adjoint trajectory volume, whose maximum values are projected onto the horizontal and vertical planes, respectively. The adjoint trajectory volumes are drawn by contours starting from a minimum value 0.02 at an interval of 0.6. The color of the contour represents how many days previous to the observation time to which the adjoint trajectory volume is associated.